Analytical Model and Concept Study of an Air Gap Fringing Shield to Reduce Losses in Gapped Inductors

Thomas Ewald, *Graduate Student Member, IEEE*, and Jürgen Biela, *Senior Member, IEEE*

***Abstract*—The impact of the magnetic fringing field emanating from the air gap in gapped inductors on the high-frequency losses has been known for a while. While most research focuses on accurately calculating these losses, attempts to reduce them through suitable measures are rare. This article investigates a concept that uses a fringing field shield to attenuate the fringing field at higher frequencies, thereby reducing losses in the winding. With this approach, losses in the shield itself occur, but the overall winding losses are reduced by 24% for an inductor subjected to a current waveform with a mixed harmonic spectrum and a dominant low-frequency component. The concept is proven using a manufactured prototype.**

***Index Terms*—Air gap, fringing field, fringing losses, gapped inductors, high frequency (HF), inductance, winding losses.**

Nomenclature

AFS	Air gap fringing shield.
RFI	Reduced fringing (field) inductor.
CI	Classical inductor (unshielded).

I. Introduction

INDUCTORS are used in many types of power electronic converters, typically with a mixed spectrum of current harmonics, where due to the high excitation currents air gaps are required to lower the effective flux density in order to avoid saturation of the core material. In these converters, the high-frequency (HF) current harmonics[1] cause significant winding losses in the inductors due to the conductors being in close vicinity to the air gap's fringing field [1]. In existing literature, the focus lies on assessing these additional losses in terms of analytical or numerical calculations [2], [3], (for instance, to consider the impact of induced losses in automated optimizations [4]), but only a few concepts are explored on how to effectively reduce these losses.

Manuscript received 4 April 2024; revised 21 June 2024; accepted 13 July 2024. Date of publication 16 July 2024; date of current version 4 September 2024. Recommended for publication by Associate Editor W. Huang. *(Corresponding author: Thomas Ewald.)*

The authors are with the Department of Information Technology and Electrical Engineering, Federal Institute of Technology, 8092 Zurich, Switzerland (e-mail: tewald@ethz.ch; jbiela@ethz.ch).

Color versions of one or more figures in this article are available at https://doi.org/10.1109/TPEL.2024.3429428.

Digital Object Identifier 10.1109/TPEL.2024.3429428

[1]In this article, a buck converter is considered as an appropriate example, which exhibits a large dc component, and a small HF component on top.

The simplest approach to reduce the fringing losses involves adding an appropriate distance between the winding and the core's center leg to reduce the impact of the fringing field on the winding [5]. The required distance can be calculated using empirical formulas. However, this additional distance leads to an increased dc resistance of the winding and a larger component in size, as the required core window recess must be considered in the design. Other attempts to place the winding around the field following the field lines [6] have shown success. The calculation of the required "clearance distance" is based on well-known formulas [7]. The presented results indicate again varying degrees of unoccupied space within the core window, depending on the considered frequency (ranging from 40% to up to 90%). In addition, the implementation of a design like the one shown in [6] is challenging in industrial manufacturing.

Efforts to redirect the air gap field away from the winding using a sheet of low-permeable material [8] also show theoretical success, but with certain limitations: The relative permeability must be in the range of 20–30 in order to not "short-circuit" the magnetic field lines, complicating the practical use of the concept, because such materials are hard to acquire [9][2] and the exact positioning of the sheet is crucial. Moreover, the additional losses and possible saturation effects in the low-permeable material are not considered, and no prototype based on the proposed concept is built, which would reveal further potential manufacturing challenges.

Finally, Fletcher et al. [10] introduced the concept of an open-circuit foil conductor (cf., Fig. 1)—in this article, termed as an Air gap fringing shield. (AFS)—to shield the winding from the air gap's fringing field. The concept is investigated using a single frequency only. FEA results indicate that the concept effectively reduces the overall winding losses of the inductor. However, the article misses the opportunity to further delve into a comprehensive concept study. As only a single frequency is considered, general statements regarding the feasibility of the concept are not possible, as shown in the following.

In order to identify its benefits, this article focuses on the concept of an AFS to reduce the impact of the air gap's fringing field on the winding losses. In this context, an AFS is an electrically

[2]In [9], not specifically the air gap field is shielded but rather the field in between individual winding layers is reduced through the use of low permeable material. It is demonstrated, that both the feasibility and practical implementation of such a concept are difficult, making especially a broader industrial application of the concept expensive or even impossible.

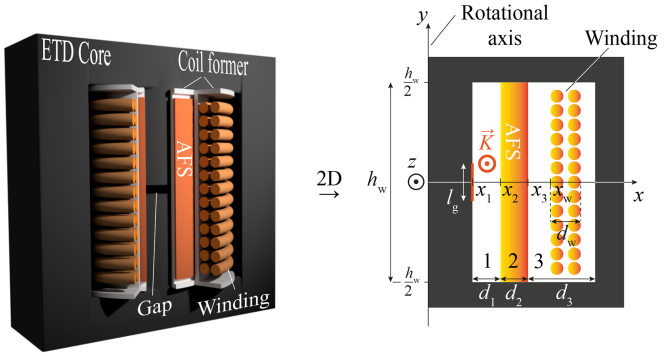

Fig. 1. Depiction of the concept: ETD core with a single air gap in the center leg, and a coil former carrying an AFS in between the center leg and the inductor's winding. In addition, the transition to the 2-D modeling concept that is used to derive the analytical model.

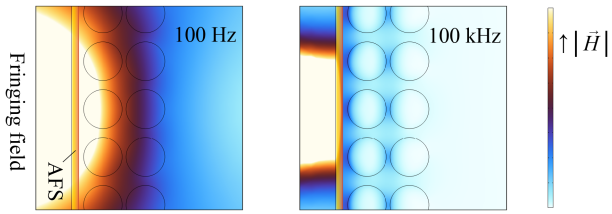

Fig. 2. Shielding effect of a 0.3 mm copper AFS in 1.5 mm distance to an air gap (FEA). Colored surface indicates magnetic field intensity (norm).

conductive foil placed between the coil former and the winding (or on a separate coil former between core and the winding's coil former), or an electrically conductive coil former (cf., Fig. 1). To ensure that the foil operates purely as an AFS, it must include a slit to prevent short circuiting (the foil effectively acts as a secondary winding). This article focuses on inductors based on E or U cores (or variants thereof), where the winding is typically wound around the gapped center leg. In such a configuration, the so-called shielding effect occurs [11]. This effect is based on the fact that the field penetrating the AFS induces eddy currents, which, according to Lenz's law, in turn create a field that opposes the original current-inducing field. As a result, the field in the AFS cancels out at high frequencies, and there is no fringing field on the side of the AFS opposite of the air gap, (cf., Fig. 2), which reduces the induced eddy current losses in the winding. However, the generated eddy currents lead to considerable losses in the AFS. An inductor carrying an AFS is termed a reduced fringing (field) (RFI) inductor in the course of this article, in contrast to a Classical inductor (unshielded) (CI). This article focuses on applying an RFI in a converter with a considerable dc current component in the inductor. In addition, one (or more) HF components are present. Since the dc resistance of the RFI remains unchanged compared to the CI, but the HF resistance of the RFI is reduced, the overall winding losses of the RFI are reduced quite significantly.

Note, that distributed gaps can be used to reduce fringing losses as well [1]. Nevertheless, distributed gaps are more difficult to manufacture and are more expensive, hence, the proposed concept is seen as an alternative to reduce the fringing losses in scenarios where cheap components are used in simple manufacturing processes. Further note that litz wire is typically used in modern designs to avoid high winding losses due to the induced eddy currents. However, also litz wire has certain disadvantages, most prominently heavily increased prices [12], a significantly lower filling factor, and consequently a larger volume (i.e., lower power density), or, as shown later in this article an increased dc resistance. Therefore, the proposed concept is seen as a low cost alternative to litz wire inductors, with comparable practicality in terms of manufacturing effort. The concept enables high power density inductors with reduced losses at the cost of adding an electrically conductive shield, which could be integrated into the coil former. The main application, as shown in this article, is in converter systems where a high dc (or LF) current with a considerable, but not too high HF ripple current, is flowing through the inductor.

In the following, a novel and comprehensive analytical model, enabling the calculation of the winding losses and the inductance of the considered RFI design, is derived and verified in Section II. Based on the model, in Section III concept studies are performed for different designs. This shows that the effectiveness of an AFS is strongly frequency dependent. Finally, the application of the concept is shown for a given current waveform with a mixed harmonic spectrum.

II. Analytical Modeling

In order to accurately describe the occurring winding losses, for instance, within the context of an optimization routine, an analytical model is necessary. In addition, since it is known that the inductance is significantly reduced through a foil conductor in close vicinity to the air gap (for a single gap configuration the inductance is reduced by approximately 25% [11]), a model for calculating the inductance must also be available. Models based on a 2-D formulation for the magnetic vector potential in the core window exist [11], [13], [14], which are utilized in the following to derive a novel and comprehensive model of an RFI. Note, that in this article only inductors with circular center legs are considered. Application of the concept is also possible to cores with rectangular center legs.

A. Magnetic Potential, Field, and Current Density

The following derivations are based on [13], and extend the model given in [13] to fully describe an inductor with the structure shown in Fig. 1. In [13], the magnetic vector potential in the core window of a gapped inductor is derived for the case of a single conductive block encapsulated by two nonconductive domains (air). It is used to describe the magnetic vector potential in the three domains shown in Fig. 1: The space between the core's center leg and the AFS (domain 1–e.g., a bobbin), the AFS (domain 2), and the shielded winding area (domain 3). This vector potential is used to derive the power losses associated with the fringing field penetrating the conductive domain. Each domain is characterized by its dedicated reference coordinate system along the x-direction starting at x_i and has its distinct width d_i. The given derivations are furthermore based on the following assumptions [13]: The core window is indefinitely

extended in z-direction; magneto-quasistatics $\rightarrow \nabla \times \vec{H} = \vec{J}$; harmonic time dependence $\frac{\partial}{\partial t} \rightarrow \mathrm{j}\omega$; shield and winding stretch from yoke to yoke; current density and vector potential have only a z-component; magnetic field has solely x and y-components.

With these assumptions, the z-component of the magnetic vector potential in each domain, denoted by the index i, is forced to satisfy to the Laplace equation within the nonconductive layers (domains 1 and 3) and the Helmholtz equation within the AFS (domain 2)

$$\nabla^2 A_{z,i} = \kappa_i^2 A_{z,i}, \quad \kappa_i^2 = \mathrm{j}\omega\sigma_i\mu_0. \tag{1}$$

In the following, ω and σ_i represent the angular frequency and the conductivity of the ith domain. Note that only in domain 2, the conductivity is nonzero and denotes the conductivity of the AFS σ_{ecs}. From that, the magnetic vector potential's formulation in the ith domain is given

$$A_{z,i} = A_{z,3}^{+} + b_{i,0}(x - x_i) + \sum_{k=0}^{\infty} \left(c_{i,k}\, \mathrm{e}^{-\xi_{i,k}(x-x_i)} + d_{i,k}\, \mathrm{e}^{\xi_{i,k}(x-x_i)} \right) \cos\left(p_k y\right). \tag{2}$$

In (2), $\xi_{i,k}^2 = \kappa_i^2 + p_k^2$, with $p_k = \frac{2\pi k}{h_{\mathrm{w}}}$. In the two subdomains from x_{w} to $x_{\mathrm{w}} + d_{\mathrm{w}}$ and from $x_{\mathrm{w}} + d_{\mathrm{w}}$ to $x_3 + d_3$, the additional magnetic vector potential $A_{z,3}^{+}$ need to be added to comply with Ampères law everywhere in the core window. The additional potential $A_{z,3}^{+}$ in (2) distinguishes the proposed model from the model in [13]. It is given according to

$$A_{z,3}^{+} = \begin{cases} -\frac{b_{3,0}}{2d_{\mathrm{w}}}(x - x_{\mathrm{w}})^2, & x_{\mathrm{w}} \leq x < x_{\mathrm{w}} + d_{\mathrm{w}} \\ -b_{3,0}\left(x - (x_{\mathrm{w}} + d_{\mathrm{w}})\right), & x_{\mathrm{w}} + d_{\mathrm{w}} < x \leq x_3 + d_3 \\ 0, & \text{elsewhere.} \end{cases} \tag{3}$$

The potential $A_{z,3}^{+}$ is required to take into account that the AFS is considered as an additional winding layer in terms of its physical properties, but there is not current flowing in the AFS. The air gap's fringing field [expressed by the infinite sum in (2)] is unaffected by $A_{z,3}^{+}$, since it only contains the total magneto-motive-force of the window, regardless of the position of the winding.

From (2), the magnetic field (x and y components in each domain) is derived based on from Ampères law, according to

$$H_{x,i} = \frac{1}{\mu_0}\frac{\partial A_{z,i}}{\partial y} \quad \wedge \quad H_{y,i} = -\frac{1}{\mu_0}\frac{\partial A_{z,i}}{\partial x}. \tag{4}$$

The magnetic field's tangential component and the magnetic flux density's normal component on the domain interfaces must be continuous at the surfaces of neighboring domains. In addition, the magnetic field's tangential component on the center leg's surface and on the outer limb's surface are known [3, Eq. (13) and (14)]. Therefore, a system of six (nine in case of $k = 0$) independent linear equations per each spatial harmonic component k [cf., (2)] can be found. The resulting systems of linear equations are solved analytically, resulting in (15) (see Appendix).

Eventually, the current density in the shield is given according to Ampères law as

$$J_{z,2} = -\frac{\kappa_2^2}{\mu_0} A_{z,2}. \tag{5}$$

B. Resistance and Inductance

When calculating the winding resistance of the inductor, it is important to consider that losses occur both in the winding and the AFS. This means that the total resistance R is composed of the following components:

$$R = R_{\mathrm{ecs}} + R_{\mathrm{w}}. \tag{6}$$

In (6), R_{w} is the actual resistance of the winding, and R_{ecs} is the additional resistance of the AFS, which is solely caused by induced eddy currents within the AFS. The calculation of the resistance of the AFS is based on (7) with the inductor current I, the winding length of the AFS around the center leg l_{ecs}, and the AFS's electrical conductivity σ_{ecs}, utilizing the current density from (5). The analytical solution of (7) is provided in

$$R_{\mathrm{ecs}} = \frac{2}{I^2} \iiint \frac{1}{2\sigma_{\mathrm{ecs}}} |J_{z,2}|^2 \, \mathrm{d}v. \tag{7}$$

The resistance of the entire winding is given in (8), where l_{w} represents the mean turn length of the winding, N the number of turns, d_{c} the conductor diameter, and σ_{w} the electrical conductivity of the winding material

$$R_{\mathrm{w}} = \frac{2Nl_{\mathrm{w}}}{\sigma_{\mathrm{w}}\pi d_{\mathrm{c}}^2} \left(\mathrm{Re}\left(\frac{\alpha \mathrm{I}_0(\alpha)}{\mathrm{I}_1(\alpha)} \right) + G_H \, \mathrm{Re}\left(\frac{\alpha \mathrm{I}_1(\alpha)}{\mathrm{I}_0(\alpha)} \right) \right). \tag{8}$$

In (8), $\alpha = (1 + \mathrm{j})\frac{d_{\mathrm{c}}}{2\delta}$ with the skin depth δ, and I_ν is the modified Bessel function of the first kind and of order ν. The HF correction factor G_H must be computed in order to evaluate the resistance of the winding. Using the analytical formulas for the magnetic field in the core window (4), G_H is calculated according to (9) [analytical solution given in the appendix (19)]

$$G_H = \frac{2}{I^2} \frac{\pi^2 d_{\mathrm{c}}^2}{d_{\mathrm{w}} h_{\mathrm{w}}} \iint_{x_{\mathrm{w}}}^{x_{\mathrm{w}}+d_{\mathrm{w}}} |\vec{H}_3|^2 \, \mathrm{d}a. \tag{9}$$

As demonstrated in [14], the total inductance of a gapped inductor is composed of the individual components of magnetic energy stored in the core L_{c}, air gap L_{g}, and winding area L_{w}, according to (10). These components can be calculated separately and then summed up

$$L = L_{\mathrm{c}} + L_{\mathrm{g}} + L_{\mathrm{w}}. \tag{10}$$

The inductance contribution of the core and air gap (neglecting the fringing effect around the air gap and considering a finite and real valued relative permeability of the core material) can be described using (11) [14]

$$L_{\mathrm{c}} + L_{\mathrm{g}} = \frac{\mu_0 k_\mu^2 N^2}{l_{\mathrm{g}}} \left(A_{\mathrm{e}} \frac{(l_{\mathrm{e}} - l_{\mathrm{g}})}{\mu_{\mathrm{r}} l_{\mathrm{g}}} + A_{\mathrm{g}} \right). \tag{11}$$

In (11), k_μ is the magnetic field strength correction factor due to the finite permeability of the core material given in (17), A_{g} is the air gap's cross-section, A_{e} is the core's effective magnetic

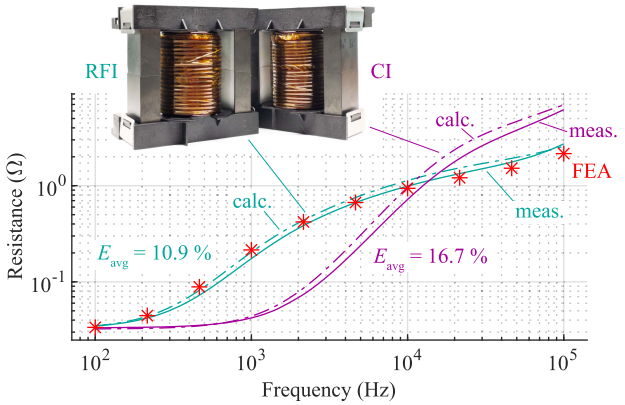

Fig. 3. Depiction of the two identically constructed 42 turn prototypes (cf., Fig. 1), one with, and one without an AFS, and the measured versus analytically calculated resistances of the two prototypes. In addition, results from an FEA simulation are shown to verify the analytical model and the assumption of negligible core losses.

cross-section, l_e is the core's effective magnetic path length, and l_g is the air gap height (cf., Fig. 1).

Calculating the inductance contribution of the core window is not straightforward, as it requires accounting for the inhomogeneous air gap fringing field. Utilizing the analytical formulation of the magnetic field (4), the inductance contribution L_w of the core window can be calculated analytically using (12) [analytical results are presented in the appendix (20)]

$$L_w = \frac{2}{I^2} \sum_{i\in\{1,2,3\}} \iiint \frac{\mu_0}{2} |\vec{H}_i|^2 \, \mathrm{d}v. \tag{12}$$

With the formulas for the resistance (6) and the inductance (10), a novel and comprehensive model for an RFI has been derived, which is used in the design concept study in Section III.

Note that the analytical model presented in this article is based on [3] and [11], which can be used to model multiple air gaps. Therefore, the proposed model in this article is capable of modeling distributed gaps, if the model is derived accordingly.

C. Impedance Analyzer Verification of the Analytical Model

The general frequency-response of a RFI is investigated using two prototypes. Impedance analyzer measurements of the two prototypes, depicted in Figs. 3 and 5, are conducted using a Keysight E4990 A impedance analyzer. The frequency-dependent resistance and inductance is extracted from the measured impedance. Capacitive effects are neglected. Both prototypes are based on an ETD 59 core [15] made of N87 MnZn ferrite with matching coil former. Solid copper wire with a diameter d_c is used for the winding. In one of the prototypes, an AFS (made of copper foil, with a slit to avoid short-circuiting) is wound directly around the coil former, and then the solid wires are applied. In the second prototype, instead of the copper shield, an equally thick Mylar film is used to maintain an identical distance between the winding and the core for both prototypes.

In the performed measurements, the average error in the RFI case is 10.9%, while the error in the CI case is 16.7%,

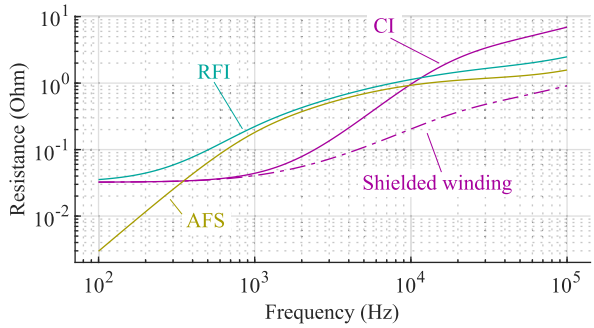

Fig. 4. Individual resistance contributions of Fig. 3 of the AFS and the winding in an RFI compared to a CI winding.

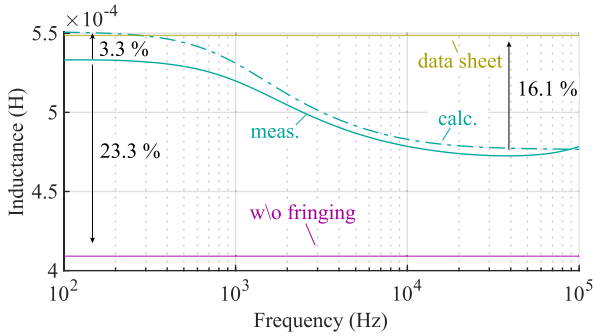

Fig. 5. Measured versus analytically calculated inductance of the RFI prototype. In addition, the inductance resulting from the A_L value from the manufacturer's data sheet [15] and the inductance without taking the fringing effect into account (11) are shown.

TABLE I
GEOMETRICAL PARAMETERS OF THE ANALYTICAL MODEL FOR THE PROTOTYPE INDUCTORS SHOWN IN FIG. 1

h_w	l_g	d_1	d_2	d_3	d_w	x_1	x_w	d_c	N
41.0	2.0	1.5	0.3	8.95	3.25	11.05	13.05	1.6	42

making the model sufficiently accurate for parameter studies and optimization tasks. The parameters for the analytical model are given in Table I (cf., Fig. 1). To use the model for a CI, the conductivity σ_{ecs} of the AFS is set to zero [e.g., Mylar, cf., (1)].The analytically calculated separate resistance contributions leading to the resistance given in Fig. 3 is shown in Fig. 4.

Since the impedance analyzer measurement may exhibit increased errors at low frequencies, an additional dc resistance measurement using a Metrel MI 3242 Ohmmeter was performed. The analytically calculated dc resistance of both inductor prototypes[3] was 35.39 mΩ, whereas the measured dc resistance of the CI was 34.80 mΩ (error of analytical model 1.7%), and the measured dc resistance of the RFI was 34.48mΩ (error of the analytical model 2.6%). The errors are well in the range of typical geometrical tolerances.

Due to the already known shielding effect [11], the inductance exhibits the expected behavior, namely a decrease in

[3]The analytical model must yield identical values at dc, since the AFS has no effect on the dc resistance.

the HF range, as shown in Fig. 5. This underlines the importance of correct analytical modeling using the model derived in Section II, as otherwise the inductance of higher harmonics in the current spectrum would be inaccurately calculated. It is evident from the measurements that neglecting the fringing effect leads to an underestimation of the inductance of 23.3% in the LF range, whereas neglecting the shielding effect while using the manufacturer's A_L value leads to an overestimation by 16.1% in the HF range. With the frequency-dependent model (10) proposed in this article, an accurate inductance calculation is possible, whereas the error in this example does not exceed 3.3%.

As shown in Fig. 3, there is a distinct difference in the behavior of the medium-frequency (MF, between 100 Hz and 20 kHz) and high-frequency (HF, above 20 kHz) resistances: The MF resistance of an RFI is greater than the resistance of a CI. The reason is that the field induces eddy currents across the full height of the AFS (cf., h_w in Fig. 1) without significant eddy current shielding [2]. Therefore, the main resistance contribution in this frequency range are the losses generated in the AFS. However, at higher frequencies, the opposite is the case, as the field gets almost entirely shielded. The induced eddy currents continue to cause high losses in the shield. However, this effect significantly reduces the area of the fringing field, resulting in much less eddy currents being induced in the entire inductor winding. Only the fringing losses induced in the AFS remain. The low-frequency ($f < 100\,\mathrm{Hz}$) resistance is unaffected by the AFS. In addition to the losses caused by the air gap field, there are, of course, skin and proximity losses in the winding due to neighboring conductors, which remain unchanged by the AFS.

D. Additional Notes on the Impedance Analyzer Measurement

To avoid strong variations of the measured values, the E4990 A impedance analyzer was configured to measure five values per frequency point and take the average of those values. In addition, multiple frequency sweeps were performed. The capacitance was neglected, therefore, the measurement was stopped at 100 kHz to avoid capacitive effects being visible in the measurement results. Neglecting the capacitance also leads to a simplified equivalent circuit, in which the inductor is modeled as a series connection of a resistor and an inductor [11], making it easily possible to extract the resistance and the inductance via the real and the imaginary parts of the impedance.

From [16], it can be concluded that the overall measurement error is below 1% between 1 kHz and 1 MHz and below 5% as long as $20\,\mathrm{Hz} < f < 1\,\mathrm{kHz}$, when measuring the impedance with the considered inductor specifications. All measurements are performed with sinusoidal small-signal excitation. Therefore, the relative permeability of the core material is assumed to be constant. The core losses are expected to be negligible in the considered scenario [14]. Therefore, the resistance can be extracted from the real part of the measured impedance. This can be further justified by the FEA results provided in Fig. 3, as they align with the measurements and the analytical model alike, indicating that the core losses are in fact negligible. The reason is that the excitation current of the impedance analyzer leads to a flux density in the core in the range of a few μT, which according to the manufacturer's data does not lead to considerable core losses (in comparison to the winding losses).

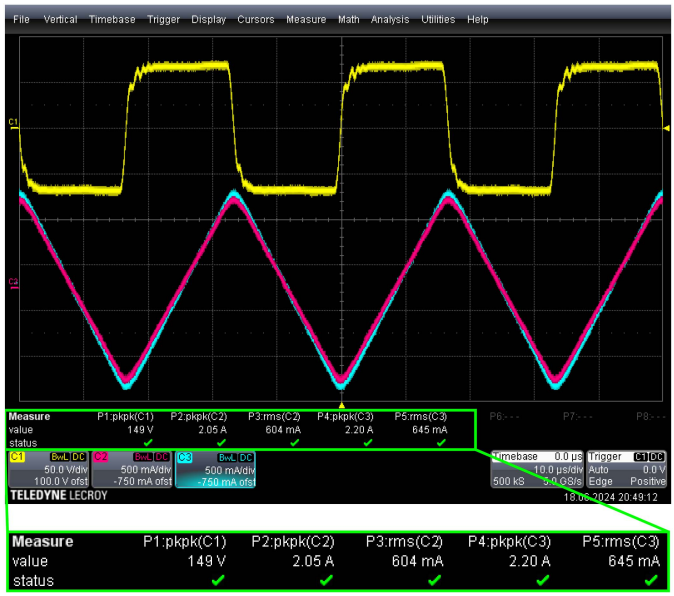

Fig. 6. Screen capture of the LeCroy Waverunner 44Xi-A showing the measured voltage (yellow) and inductor currents (blue: RFI, purple: CI).

TABLE II
MEASURED INDUCTOR VOLTAGE AND CURRENTS

	Voltage	Current pk-pk	Current rms	Current offset
CI	150 V	2.05 A	604 mA	−750 mA
RFI	150 V	2.20 A	645 mA	−750 mA

E. Thermal Verification of the Analytical Model

The concept is further proven by an analysis of the temperature rise of the individual inductor prototypes. Measuring the temperature allows for more accurate conclusions about the losses incurred because the impedance analyzer measures the impedance, but not the actual ohmic resistance. As a result, resistance measurements can have high errors when phase angles are close to 90° (i.e., at high frequencies).

Both inductors were placed next to each other and connected in parallel to an AE Techron 7228 linear power amplifier, controlled with an Agilent 33500 signal generator, which was used to create a rectangular voltage waveform (identical to the voltage across the inductor in a buck converter with duty cycle of 0.5). The voltage amplitude was 150 V pk-pk (cf., Fig. 6, C1). The switching frequency was set to 30 kHz, which results in ac resistances of 1.5 Ω of the RFI and 2.6 Ω of the CI, as shown in Fig. 3.

Voltage and inductor currents were measured with a LeCroy ADP305 voltage probe and 2 LeCroy CP030 current probes using a LeCroy Waverunner 44Xi-A oscilloscope. The measurements results are given in Table II. The difference in the inductor currents originates from the fact, that the shielding inductor has

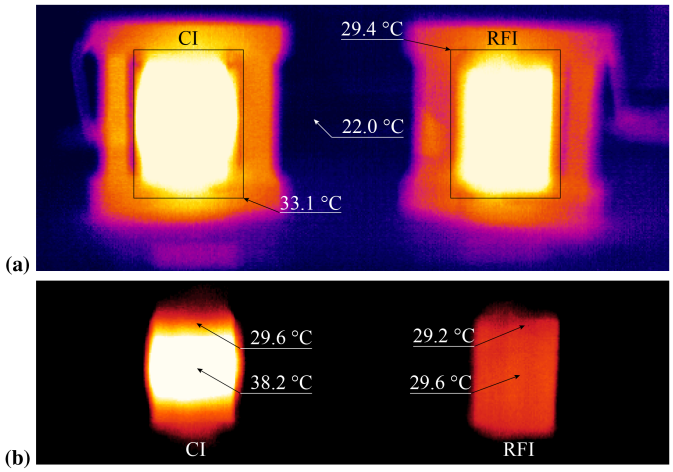

Fig. 7. Thermal images captured with an Optris PI640, showing the CI on the left, and the RFI on the right. (a) Image of both inductor prototypes showing the ambient temperature and average temperatures of the windings, and (b) the same image with different color scaling, to better highlight the temperature distribution across the winding surface of both prototypes.

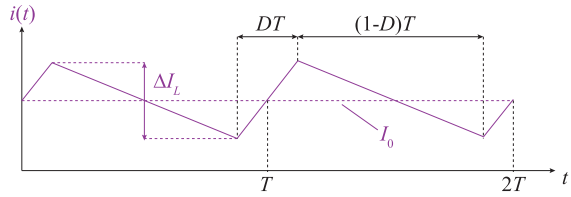

Fig. 8. Current waveform of the inductor current with $T = 1/f_s$.

TABLE III
CURRENT WAVEFORM

f_s (kHz)	T (μs)	D (-)	I_0 (A)	ΔI (A)	V_1 (V)	V_2 (V)
20	50	0.5	8.33	2.5	48	24

TABLE IV
PARAMETERS FOR AREA PRODUCT CALCULATION

L (μH)	B_{max} (mT)	J_{max} (A mm^{-2})	k_w (-)
240	250	5	0.4

a slightly reduced inductance at 30 kHz (cf., Fig. 5), resulting in a slightly increased ripple current for the shielding inductor. To verify the temperature rise, the inductors were operated under the aforementioned conditions for 30 min. The thermal equilibrium was reached after 10 min. An infrared Optris PI640 thermal camera was used to capture the thermal images of both inductors.

The thermal images [cf., Fig. 7(a) and (b)] were inspected using the software PIX Connect, which enables a pointwise evaluation of the temperatures that are captured. For the CI, the evaluation revealed a hotspot temperature rise above room temperature (22°) of 16.2° in the middle of the winding, and an average temperature rise of the whole winding of 11.1°. The RFI only exhibited a hotspot temperature rise of 7.6°, while the average temperature rise was measured to be 7.4°.

Interestingly, the RFI not only achieved a measurably lower temperature, but also showed a noticeably more homogeneous temperature distribution across the winding [cf., Fig. 7(b)]. The reason for this lies in the spatially strongly inhomogeneous fringing losses, which are in case of the RFI entirely absorbed by the AFS. The AFS has a higher thermal conductivity in the axial direction compared to the winding pack, allowing the heat to distribute more evenly. All this was achieved even though the RFI was subjected to a slightly higher current than the CI, proving that the concept presented in this article can achieve lower loss inductors using an AFS.

III. DISCUSSION

In this section, possible application scenarios for the AFS are discussed based on the proposed model as a beneficial use of the AFS strongly depends on the considered frequency. The starting point is the design of an inductor based on a classical design procedure, as for example given in [17]. Here, the inductor current is assumed to be given. Then, the potential winding loss reduction by using an AFS is illustrated using the analytical model. In addition, the determined design is used to conduct further phenomenological studies to unveil general tradeoffs of a RFI design.

In general, it can be noted that an AFS is best suited for the use in high-current inductors with current waveforms containing a high dc (or low frequency) components, in addition to a HF ripple. Due to the high dc current, usually a wire with a high current carrying capacity is chosen, leading to a relatively large wire cross section. This makes the winding susceptible eddy currents caused by the fringing field associated with the HF component of the current. An AFS effectively neglects the fringing field impact on the conductors at high frequencies, by shielding the fringing field.

It is to note, that the application of an AFS is taylored to scenarios where the shield is placed as close to the core's center leg as possible, to remain a minimal dc resistance of the inductor winding. Concepts of increasing the distance between core and winding are evaluated in the introduction of this article, and are not the scope of this article.

A. Application Example of An AFS

The following example is a scenario for an inductor, which is exposed to a mixed current waveform with harmonics (cf., Fig. 8). Such a current waveform can occur in, e.g., a buck converter [18]. The considered waveform specifications are presented in Table III. Based on this current waveform, the required inductance is determined. The procedure for a CI design follows the design methodology described in [17], utilizing the so-called area product, which is the product of the core's cross-section A_c and the core window cross-section A_w. Values for calculating the area product are taken from Table IV, where the chosen material is N87.Based on the procedure given in [17], an ETD 44/22/15 core is chosen.

In the following, two designs are compared: The classical design and an RFI based on the classical design, with the only difference being an AFS placed in between core and winding.

TABLE V
GEOMETRICAL PARAMETERS OF THE ANALYTICAL MODEL FOR THE THEORETICAL EXAMPLE INDUCTOR

h_w	l_g	d_1	d_2	d_3	d_w	x_1	x_w	d_c	N
32.2	4.0	0.25	0.5	7.95	7.7	7.6	8.6	1.7	51

*All parameters in mm, except the number of turns N.

TABLE VI
RELEVANT CURRENT HARMONICS OF THE INDUCTOR CURRENT

n	0	1	3	5	7
nf_s (kHz)	0	20	60	100	140
I_n (A)	8.33	1.0	-0.1	0.04	-0.02

TABLE VII
THEORETICAL CALCULATION RESULTS FOR BOTH INDUCTOR DESIGNS

	P_0 (W)	P_1 (W)	P_w (W)	P_c (W)	P_{tot} (W)
CI	2.12	2.16	4.27	0.09	4.36
RFI	2.12	0.88	3.01	0.09	3.10

TABLE VIII
THEORETICAL CALCULATION RESULTS FOR BOTH INDUCTOR DESIGNS—THE RFI'S GAP IS ADJUSTED TO ACHIEVE THE REQUIRED INDUCTANCE

	P_0 (W)	P_1 (W)	P_w (W)	P_c (W)	P_{tot} (W)
CI	2.12	2.16	4.27	0.09	4.36
RFI	2.12	1.11	3.24	0.09	3.33

It is assumed that the AFS can be positioned in such a way that the winding remains at the same place, meaning that in both designs, RFI and CI, the distance x_w (cf., Fig. 1) is the same (cf., Table V).This can be achieved, if the AFS is integrated into the coil former, which also provides improved thermal properties, since the shield has a high thermal conductivity, and the remaining winding losses of the active winding can be dissipated through the coil former better. A more comprehensive thermal analysis is not part of this article. In addition to the winding losses, the analysis covers the core losses P_c, which are computed for the given excitation using the iGSE [19]:

$$P_c = V_e \frac{k_i \left(\Delta B\right)^{\beta}}{T} \sum_j \left(\Delta t_j\right)^{1-\alpha}$$

with the effective magnetic volume of the core V_e. The flux density swing is computed from the inductor voltage as

$$\Delta B = \frac{DT}{NA_e} \left(V_1 - V_2\right).$$

Since the core, the number of turns, and the voltage across the inductors are the same in all scenarios, all of the following example inductors exhibit the same core losses. The total losses P_{tot} are then given as the sum of core and winding losses.

The inductor's real-valued current waveform is decomposed into a Fourier series as

$$i_L = I_0 + \sum_{n=1}^{\infty} \underbrace{-\Delta I_L \frac{\sin(\pi n D)}{n^2 \pi^2 (D^2 - D)}}_{I_n} \sin\left(2\pi n f_s t\right). \quad (13)$$

The five highest current harmonics for the following calculations are listed in Table VI.

To compare both designs, the overall winding losses are computed using (14). There, only the dc ($n = 0$) and the fundamental component ($n = 1$) of the current must be considered (cf., Table VI)

$$P_w = R_0 I_0^2 + \frac{1}{2} \sum_{n=1}^{\infty} R_n I_n^2 \approx \underbrace{R_0 I_0^2}_{P_0} + \underbrace{\frac{1}{2} R_1 I_1^2}_{P_1}. \quad (14)$$

The results for both designs are given in Table VII.

For this specific example, the relative total loss reduction of the RFI is a bit less than 30%. This is achieved, because the HF loss component P_1 is reduced by 60%. The core losses play a minor role, since the specific current waveform of the buck converter does not exhibit high flux density swings in the core, leading to generally low core losses.

A general quantitative statement about the potential winding loss reduction is not possible, as the overall winding losses are determined by a sum of the individual loss components for each current harmonic, weighted by the frequency-dependent resistances [cf., (14)]. For this reason, having an analytical model available for calculating an RFI design is crucial. This model allows for a quick and reliable estimation of the winding losses during the design phase to determine if the use of an AFS is beneficial.

B. Note on the Inductance Variation Due to the Shielding Effect

Due to the shielding effect at higher frequencies, the inductance exhibits a notable frequency-dependence (cf., Fig. 5). This leads to the actual inductance differing from the required inductance computed based on the area-product design procedure. In the given example, the inductance at 20 kHz is reduced to 160 μH (calculated using the analytical model). In order to achieve the required inductance of 240 μH, the air gap length of the RFI is reduced from 4.0 to 2.6 mm. This does not affect the previous design procedure. However, a smaller air gap results in different winding losses. Recalculation of the winding losses of the RFI reveals that the RFI design still exhibits 23% less total losses than the CI, as shown in Table VIII.

C. Note on the Use of HF Litz-Wire

To reduce HF winding losses when constructing inductors exposed to a HF current spectrum, usually HF litz-wire is used. In case HF litz-wire is used, an AFS would not prove to be beneficial, as the majority of the winding losses are exhibited by the AFS itself (cf., Fig 4). Furthermore, in case HF litz-wire is used, a HF litz-wire with the same outer diameter as a solid wire typically has an inner copper fill factor in the range of 0.5 [20]. Hence, replacing solid wires with HF litz-wire with the same outer diameter would result in halving the copper cross-sectional area, and a doubling of the dc resistance. Table IX shows the previously calculated inductor examples, and in addition, an

TABLE IX
THEORETICAL CALCULATION RESULTS FOR THREE INDUCTOR DESIGNS—THE CI, THE RFI, AND AN ADDITIONAL LITZ WIRE INDUCTOR

	P_0 (W)	P_1 (W)	P_w (W)	P_c (W)	P_{tot} (W)
CI	2.12	2.16	4.27	0.09	4.36
RFI	2.12	1.11	3.24	0.09	3.33
Litz	4.25	0.04	4.29	0.09	4.38

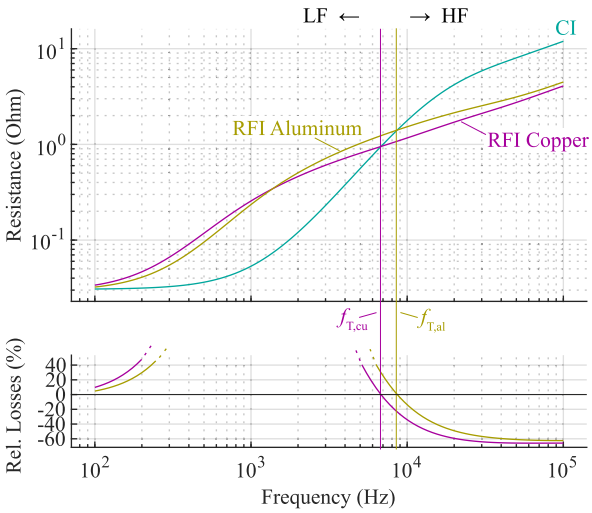

Fig. 9. Frequency-dependent resistance of the RFI using a copper and an aluminium AFS compared to the CI and relative loss reduction vs. frequency.

inductor employing litz wire instead of solid wire. Litz wire with a strand diameter of 0.1 mm and an inner filling factor of 0.5 was assumed. The winding losses were calculated using models from [14]. As can be seen, the litz wire inductor does not exhibit significant ac winding losses, however, doubled dc winding losses. However, in this case the maximum allowed current density would be exceeded (this would lead to overheating of the winding), making this design invalid. On the other hand, repeating the design procedure using the area product [17] and taking into account the inner fill factor of 0.5, the required area product would be doubled. This leads to a significant increase of the inductor volume by approximately 70% (factor $2^{3/4}$). Therefore, the power density decreases significantly. Because of these tradeoffs (volume, power density, versus overall losses) such a design cannot be compared to the presented inductors just in terms of its power losses, as additional factors like cost, available space, weight, etc., must be considered. A comprehensive tradeoff analysis is required and is retained for future publication.

D. Impact of the AFS Material on the Winding Resistance

As already shown in Section II, an RFI exhibits a different frequency dependence of the winding resistance. Fig. 9 illustrates the frequency-dependent resistances of different designs based on the previous section (cf., Table V): a CI, one with a 0.5 mm copper AFS, and one with a 0.5 mm aluminum AFS. As can be seen, significantly increased overall winding losses occur in all designs at low to medium frequencies. Generally, a higher

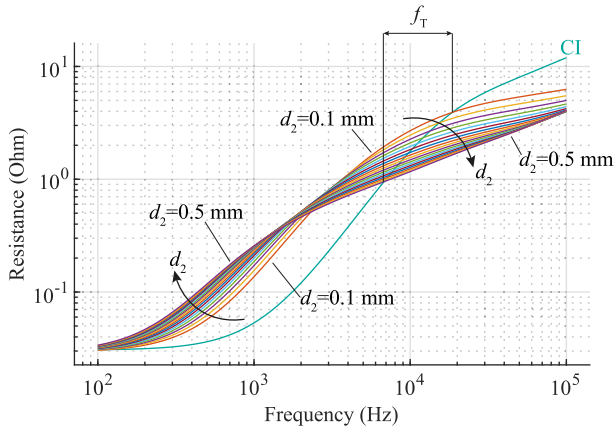

Fig. 10. Frequency-dependent resistance of the example inductor with different copper AFS widths $0.1\text{mm} \leq \text{d}_2 \leq 0.5\text{mm}$.

conductivity of the AFS results in a better manifestation of the shielding effect. In the considered cases, frequency-dependent winding loss reduction by up to −60% is possible. From Fig. 9 it can be concluded, that there is a so-called transition frequency[4] f_T, where the RFI exhibits a lower total winding resistance compared to a CI design. In order to benefit from the shielding effect, the frequency must be higher than f_T (in case of a purely sinusoidal current at only a single frequency), or the majority of the current's harmonic spectrum must be near dc and at frequencies higher than f_T. Consequently, the shielding effect can be beneficially leveraged in windings that are subject to current waveforms with this specific property (e.g., a dc current with HF ripple, occurring, for example, in a Buck converter, as shown in this example).

E. Impact of the AFS Thickness on the Eddy Current Losses

Fig. 10 shows the behavior of a CI, as well as a series of resistance curves of an RFI equipped with a copper AFS, varying in thickness from 0.1 to 0.5 mm. This results in a change of the resistance curves with frequency. It can be observed that a thicker AFS generally leads to less winding losses in the HF range. In addition, the transition frequency f_T is shifted to a lower frequency. On the other hand, an excessively thick AFS requires too much space and can significantly increase the component's cost. The optimum AFS thickness is therefore the maximum reasonable AFS thickness in terms of manufacturing and cost.

In addition to the noticeable advantage of having a thicker AFS, there is a question about the minimum thickness. Almost complete shielding occurs as soon as the AFS is thicker than the skin depth, which depends on the frequency and the material parameters. Therefore, a guideline can be given that

$$d_2 \geq \delta = \left(\pi f_{ms} \sigma_{ecs} \mu_0\right)^{-1/2}$$

[4]The transition frequency is used here to illustrate the concept. However, it is not possible to compute the transition frequency beforehand, since the analytical model cannot be reformulated to compute this frequency. Furthermore, f_T depends on both, the AFS's thickness and the conductor diameter d_c itself.

where f_{ms} (ms: "most significant") represents the frequency of the lowest HF current component with a significant amplitude. In this example, f_{ms} is the switching frequency f_{s}. For this frequency, the skin depth in copper is 0.46 mm.

IV. Conclusion

In this article, the concept of an AFS is applied to gapped inductors to reduce the impact of the air gap's fringing field on the inductor's winding. A novel analytical model is proposed and used to compute the power losses and the inductance of an inductor with AFS over a wide frequency range. The calculation results are compared to measurement results, revealing a very high accuracy of the model (within 11% error). The measurements prove that an AFS can reduce the winding losses in inductors.

Based on the analytical model, an example of a RFI is provided to show the relative loss reduction in the context of a current with a mixed harmonic spectrum. Results are presented, which indicate the beneficial use of an AFS in this context, by showing a loss reduction of 24%. Leveraging the proposed model enables quick and reliable estimation of the winding losses during the design phase to determine whether the utilization of an AFS is beneficial. A fast and accurate design and optimization of inductors with AFS for different converter applications is therefore enabled.

Appendix

Coefficients

Here, the solution for the spatial coefficients, resulting from the resolution of the system of linear equations, described in Section II are given

$$
\begin{aligned}
b_{1,0} &= b_{3,0} = \frac{\mu_0 N I}{h_{\mathrm{w}}} \\
b_{2,0} &= c_{1,0} = c_{3,0} = d_{1,0} = d_{3,0} = 0 \\
c_{2,0} &= -\mathrm{e}^{\kappa_2 d_2}\, d_{2,0} = \frac{\mu_0 N I}{\kappa_2 h_{\mathrm{w}}} \frac{\mathrm{e}^{\kappa_2 d_2}}{\mathrm{e}^{\kappa_2 d_2}+1} \\
c_{1,k} &= -\frac{B_k}{D_k}\left(p_k^2\eta_1 - \xi_k^2\eta_1 - p_k^2\eta_1\eta_2 - p_k^2\eta_1\eta_3\right. \\
&\quad - \xi_k^2\eta_1\eta_2 + \xi_k^2\eta_1\eta_3 + p_k^2\eta_1\eta_2\eta_3 + \xi_k^2\eta_1\eta_2\eta_3 \\
&\quad \left. + 2p_k\xi_k\eta_1\eta_2 + 2p_k\xi_k\eta_1\eta_2\eta_3\right) \\
d_{1,k} &= -\frac{B_k}{D_k}\left(p_k^2 + \xi_k^2 - p_k^2\eta_2 - p_k^2\eta_3 + \xi_k^2\eta_2 - \xi_k^2\eta_3\right. \\
&\quad \left. + 2p_k\xi_k + 2p_k\xi_k\eta_3 + p_k^2\eta_2\eta_3 - \xi_k^2\eta_2\eta_3\right) \\
c_{2,k} &= -\frac{2p_k B_k}{D_k}\eta_4(\xi_k\eta_3 - p_k\eta_3 + p_k\eta_2\eta_3 + \xi_k\eta_2\eta_3) \\
d_{2,k} &= -\frac{2p_k B_k}{D_k}\eta_4(p_k + \xi_k - p_k\eta_2 + \xi_k\eta_2) \\
c_{3,k} &= \eta_2 d_{3,k} = -\frac{4p_k B_k}{D_k}\xi_k\eta_2\eta_4\eta_5
\end{aligned}
\tag{15}
$$

The variables used in (15) are provided as

$$
\begin{aligned}
D_k &= 2p_k\xi_k - p_k^2\eta_1 - p_k^2\eta_2 + p_k^2 + \xi_k^2\eta_1 - p_k^2\eta_3 \\
&\quad + \xi_k^2\eta_2 + \xi_k^2 - \xi_k^2\eta_3 + p_k^2\eta_1\eta_2 + p_k^2\eta_1\eta_3 + \xi_k^2\eta_1\eta_2 \\
&\quad + p_k^2\eta_2\eta_3 - \xi_k^2\eta_1\eta_3 - \xi_k^2\eta_2\eta_3 + 2p_k\xi_k\eta_3 - p_k^2\eta_1\eta_2\eta_3 \\
&\quad - \xi_k^2\eta_1\eta_2\eta_3 - 2p_k\xi_k\eta_1\eta_2 - 2p_k\xi_k\eta_1\eta_2\eta_3 \\
\eta_1 &= \mathrm{e}^{2d_1 p_k} \qquad \eta_2 = \mathrm{e}^{2d_3 p_k} \qquad \eta_3 = \mathrm{e}^{2d_2\xi_k} \\
\eta_4 &= \mathrm{e}^{d_1 p_k} \qquad \eta_5 = \mathrm{e}^{d_2\xi_k} \\
B_k &= -\frac{4\mu_0 H_{\mathrm{g}}}{p_k^2 h_{\mathrm{w}}} \sin\left(\frac{p_k l_{\mathrm{g}}}{2}\right).
\end{aligned}
\tag{16}
$$

The magnetic field strength in the air gap H_{g}, which is used in (16), is calculated based on the assumption that the field is spatially homogeneous inside the gap, has only a y-component, and that the core material has a relative permeability of $\mu_{\mathrm{r}} \gg 1$, resulting in (17) [14]

$$
H_{\mathrm{g}} = k_\mu \frac{NI}{l_{\mathrm{g}}}, \qquad k_\mu = \left(1 + \frac{l_{\mathrm{e}} - l_{\mathrm{g}}}{\mu_{\mathrm{r}} l_{\mathrm{g}}}\right)^{-1}. \tag{17}
$$

Resistance calculation in the AFS: The resistance of the AFS is analytically computed based on (7). Hereby, as well as when solving (20), the integrals are solved in polar coordinates, since the used ETD core has a circular center leg. The same procedure can be applied to cores with rectangular center legs, where the integrals must be solved in Cartesian coordinates [3]

$$
\begin{aligned}
R_{\mathrm{ecs}} &= \frac{\pi\omega^2\sigma_{\mathrm{ecs}} h_{\mathrm{w}}}{I^2} \\
&\quad \times \left(\sum_{k=0}^{\infty} |c_{2,k}|^2\eta_{1,2,k} + 2c_{2,k}d_{2,k}^{*}\eta_{2,2,k} + |d_{2,k}|^2\eta_{3,2,k}\right).
\end{aligned}
\tag{18}
$$

The coefficients $\eta_{j,i,k}$, $\xi'_{i,k}$, and $\xi''_{i,k}$ are given in (20) for $i = 2$.

Proximity losses in the inductor winding caused by the fringing field: The impact of the magnetic field on the proximity losses of the inductor winding are analytically computed using

$$
\begin{aligned}
G_H &= \frac{2\pi^2 d_{\mathrm{c}}^2}{\mu_0^2 I^2} \\
&\quad \times \left(\frac{b_{3,0}^2}{3} + \frac{1}{d_{\mathrm{w}}}\sum_{k=1}^{\infty} p_k^2\left(|c_{3,k}|^2\eta_{1,3,k} + |d_{3,k}|^2\eta_{3,3,k}\right)\right) \\
\eta_{1,3,k} &= \frac{\mathrm{e}^{-2p_k(x_{\mathrm{w}}+d_{\mathrm{w}}-x_3)}}{-2p_k} - \frac{\mathrm{e}^{-2p_k(x_{\mathrm{w}}-x_3)}}{-2p_k} \\
\eta_{3,3,k} &= \frac{\mathrm{e}^{2p_k(x_{\mathrm{w}}+d_{\mathrm{w}}-x_3)}}{2p_k} - \frac{\mathrm{e}^{2p_k(x_{\mathrm{w}}-x_3)}}{2p_k}.
\end{aligned}
\tag{19}
$$

Inductance calculation considering the fringing field: The inductance of the inductor considering the fringing field of the air gap is analytically calculated based on

$$
L_{\mathrm{w}} = \frac{\pi h_{\mathrm{w}}}{\mu_0 I^2}
$$

$$\times \left(\sum_{i\in\{1,2,3\}} \left(p_k^2 + |\xi_{i,k}|^2\right) |c_{i,k}|^2 \eta_{1,i,k} + 2\left(p_k^2 - |\xi_{i,k}|^2\right) c_{i,k} d_{i,k}^* \eta_{2,i,k} + \left(p_k^2 + |\xi_{i,k}|^2\right) |d_{i,k}|^2 \eta_{3,i,k} \right)$$

$$\eta_{1,i,k} = \frac{\mathrm{e}^{-2\xi'_{i,k}d_i}\left(-2\xi'_{i,k}\left(x_i+d_i\right)-1\right)}{\left(-2\xi'_{i,k}\right)^2} - \frac{-2\xi'_{i,k}x_i - 1}{\left(-2\xi'_{i,k}\right)^2}$$

$$\eta_{2,i,k} = \frac{\mathrm{e}^{-2\mathrm{j}\xi''_{i,k}d_i}\left(-2\mathrm{j}\xi''_{i,k}\left(x_i+d_i\right)-1\right)}{\left(-2\mathrm{j}\xi''_{i,k}\right)^2} - \frac{-2\mathrm{j}\xi''_{i,k}x_i - 1}{\left(-2\mathrm{j}\xi''_{i,k}\right)^2}$$

$$\eta_{3,i,k} = \frac{\mathrm{e}^{2\xi'_{i,k}d_i}\left(2\xi'_{i,k}\left(x_i+d_i\right)-1\right)}{\left(2\xi'_{i,k}\right)^2} - \frac{2\xi'_{i,k}x_i - 1}{\left(2\xi'_{i,k}\right)^2}$$

$$\xi'_{i,k} = \xi_{i,k} \qquad \xi''_{i,k} = \mathrm{Im}\left(\xi_{i,k}\right). \tag{20}$$

Note, that in the above formula, $\xi_{i,k} = p_k$ in domain 1 and 3 (cf., Fig. 1), which significantly simplifies the resulting expression for the inductance contribution of these regions.

Also note, that the inductance formula (20) does not contain the 1-D leakage field, because its contribution to the total inductance in case of a gapped inductor is negligible [14].

REFERENCES

[1] R. Severns, "Additional losses in high frequency magnetics due to non ideal field distributions," in *Proc. 7th Annu. Appl. Power Electron. Conf. Expo.*, 1992, pp. 333–338.

[2] D. Leuenberger and J. Biela, "Semi-numerical method for loss calculation in foil windings exposed to an air gap field," in *Proc. Int. Power Electron. Conf.*, 2014, pp. 868–875.

[3] T. Ewald and J. Biela, "Analytical eddy current loss model for foil conductors in gapped cores," in *Proc. 23th Eur. Conf. Power Electron. Appl.*, 2021, pp. 1–10.

[4] P. Wallmeier, N. Frohleke, and H. Grotstollen, "Automated optimization of high frequency inductors," in *Proc. 24th Annu. Ind. Electron. Soc. Conf.*, 1998, pp. 342–347.

[5] V. C. Valchev and A. V. den Bossche, *Inductors and Transformers for Power Electronics*. Boca Raton, FL, USA: CRC Press, 2005.

[6] J. Hu and C. R. Sullivan, "Optimization of shapes for round wire, high frequency gapped inductor windings," in *Proc. 33rd IEEE Ind. Appl. Conf.*, 1998, pp. 907–912.

[7] C. Sullivan, "Winding loss calculation with multiple windings, arbitrary waveforms, and two-dimensional field geometry," in *Proc. Conf. Rec. 34th Ind. Appl. Conf.*, 1999, pp. 2093–2099.

[8] X. Mao, W. Chen, and Y. Li, "Winding loss mechanism analysis and design for new structure high-frequency gapped inductor," *IEEE Trans. Magn.*, vol. 41, no. 10, pp. 4036–4038, Oct. 2005.

[9] P. Wallmeier and H. Grotstollen, "Magnetic shielding applied to high-frequency inductors," in *Proc. Rec. 32nd Ind. App. Conf.*, 1997, pp. 1131–1138.

[10] J. Fletcher, B. Williams, and M. Mahmoud, "Airgap fringing flux reduction in inductors using open-circuit copper screens," *Proc. Elect. Power Appl.*, vol. 152, pp. 990–996, 2005.

[11] T. Ewald and J. Biela, "Frequency-dependent inductance and winding loss model for gapped foil inductors," *Trans. Power Electron.*, vol 37, pp. 12370–12379, 2022.

[12] R. Burkart and J. W. Kolar, "Component cost models for multi-objective optimizations of switched-mode power converters," in *Proc. IEEE Energy Convers. Congr. Expo.*, 2013, pp. 2139–2146.

[13] P. Wallmeier, N. Frohleke, and H. Grotstollen, "Improved analytical modeling of conductive losses in gapped high-frequency inductors," in *Proc. 33rd Ind. Appl. Soc. Conf.*, 1998, pp. 913–920.

[14] T. Ewald and J. Biela, "Analytical winding loss and inductance models for gapped inductors with litz or solid wires," *IEEE Trans. Power Electron.*, vol. 37, no. 12, pp. 15127–15139, Dec. 2022.

[15] *Ferrites and Accessories—ETD 59/31/22*, Chuo City, Tokyo, Japan: TDK, 2017.

[16] *Keysight E4990 A Impedance Analyzer*, Santa Rosa, CA, USA: Keysight, 2018.

[17] C. W. T. McLyman and A. P. Wagner, "Designing high frequency AC inductors using ferrite and molypermalloy powder cores (MPP)," in *Proc. Power Electron. Specialists Conf.*, 1985, pp. 171–175.

[18] F. Zach, *Leistungselektronik*. Wiesbaden, Germany: Springer, 2015.

[19] K. Venkatachalam, C. Sullivan, T. Abdallah, and H. Tacca, "Accurate prediction of ferrite core loss with nonsinusoidal waveforms using only Steinmetz parameters," in *Proc. Workshop Comput. Power Electron.*, 2002, pp. 36–41.

[20] A. Rosskopf and C. Brunner, "Enhancing litz wire power loss calculations by combining a sparse strand element equivalent circuit method with a Voronoi-based geometry model," *IEEE Trans. Power Electron.*, vol. 37, no. 9, pp. 11450–11456, Sep. 2022.

Thomas Ewald (Graduate Student Member, IEEE) studied electrical engineering with focus on Energy Conversion Technology from the Technical University of Munich (TUM), Munich, Germany. He received the B.Sc. and M.Sc. degrees in electrical engineering from TUM in 2015 and 2018, respectively. He is currently working toward the Ph.D. degree with the Laboratory for High Power Electronic Systems, ETH Zurich, Zurich, Switzerland.

In 2017, he wrote his master's thesis at BMW AG in the R&D department for electrical drive components. In his master's thesis he developed an analytical model for simulating transient processes in both, permanent magnet and electrically excited synchronous machines.

Jürgen Biela (Senior Member, IEEE) received the Diploma (hons.) degree in electrical engineering from Friedrich-Alexander Universität Erlangen-Nürnberg, Erlangen, Germany, in 1999, and the Ph.D. degree in electrical engineering from the Swiss Federal Institute of Technology (ETH), Zürich, Switzerland, in 2006.

In 2000, he joined the Research Department, Siemens A&D, Erlangen, and in 2002, he joined the Power Electronic Systems Laboratory, ETH Zürich, as a Ph.D. Student focusing on electromagnetically integrated resonant converters, where he was a Postdoctoral Fellow from 2006 to 2010. Since 2010, he has been an Associate Professor, and since 2020, a Full Professor of high-power electronic systems with ETH Zurich.